Phonon-Fluid Coupling Enhanced Water Desalination in Flexible 2D Porous Membranes

*Yechan Noh and N. R. Aluru**

Department of Mechanical Science and Engineering, University of Illinois at Urbana-Champaign, Urbana, Illinois 61801, United States

* Walker Department of Mechanical Engineering, Oden Institute for Computational Engineering and Sciences, The University of Texas at Austin, Austin 78712, United States

* *Correspondence should be addressed to aluru@utexas.edu*

KEYWORDS

Water desalination, nanopores, 2D materials, graphene nanomesh, covalent-organic-frameworks, metal-organic-frameworks, flexible membrane, phonon-fluid coupling, mechanosensitive membranes, molecular dynamics, nanofluidics

ABSTRACT

Water purification using 2D nanoporous membranes has been drawing significant attention for over a decade because of fast water transport in ultrathin membranes. We perform a comprehensive study using molecular dynamics (MD) simulations on water desalination using 2D flexible membranes where the coupling between the fluid dynamics and mechanics of the membrane plays an important role. We observe that a considerable deformation and fluctuation in the 2D membrane results in an enhanced water permeability (up to 122%) along with a slight decrease in the salt rejection rate (less than 11%). Simulations on harmonically vibrating membranes indicate that the vibrational match at the membrane-water interface can significantly increase the permeance. We conduct mechanical stability tests and discuss the maximum endurable pressure of 2D porous membranes for water desalination. These findings will contribute to advances in applications using ultra-thin membranes, such as energy harvesting and molecular separation.

INTRODUCTION

The mechanical flexibility and thermal fluctuations of materials are ubiquitous and fundamental to many physical phenomena. In nanoscale biophysics, thermal fluctuations are an important mechanism for molecular transport in biological channels[1,2] and the catalytic activity of enzymes[3]. In human-made systems, the thermal fluctuations of surfaces are known to affect the wetting properties[4], the diffusion coefficient of interfacial fluids[5,6], and thus the fluid transport[5–7]. These effects are no exception for water desalination using 2D nanoporous membranes, which can exhibit high mechanical flexibility owing to their atomically thin thickness and high porosity[8–10]. Notably, the scale of thermal fluctuations of a 2D membrane (*e.g.,* 0.07 ~ 2.0 nm in graphene[11,12]) is comparable to the size of the pores (~ 0.5 nm)[13] of desalination membranes. Thus, it is important to understand how the flexibility of the membrane influences the filtration performance.

Water desalination using 2D nanoporous membranes provides an efficient route for production of clean water at a low energy cost with simple mechanisms[13]. This process utilizes reverse osmosis (RO), where mechanical energy is applied to the system to generate water permeation through the membrane by filtering out unwanted molecular species. Filtering ionic species takes advantage of the fact that the size of the water molecule (~ 0.3 nm) is smaller than that of the hydrated ions (0.6 ~ 1.0 nm)[14]. For a high rejection rate, the pore size must be kept smaller than the effective size of the ion. On the other hand, the production of clean water increases with the size of the pore diameter. For optimal desalination performance, it is important to ensure a consistent pore size throughout the membrane[15].

Nanoporous graphene membrane is one of the most widely studied 2D material for water desalination. The fabrication of graphene nanopores has, for decades, relied on top-down

methods such as drilling graphene using a focused ion beam or exposing graphene to oxygen plasma; thus, fabricating large-scale nanoporous graphene with a consistent pore size was challenging. Recently, Moreno *et al.*[16] successfully fabricated a large-scale nanoporous graphene membrane with a consistent pore size using the self-assembly of graphene nanoribbons—namely, a graphene nanomesh (GNM). Yang *et al.*[15] experimentally demonstrated large-scale water purification using GNM reinforced by carbon nanotube networks. Other types of porous membranes have also been synthesized by the bottom-up approach. The covalent-organic framework (COF)[17,18] has been widely studied for various applications such as energy storage[19] and membrane separations[20] because of its lightweight and high porosity. Water desalination using 2D COF was computationally examined by Lin *et al*. in 2015.[21] They showed that the covalent triazine-based framework (CTFs), one of the 2D COFs, is an ideal candidate for water desalination. The metal-organic framework (MOF)[22], a porous material linked by metallic-organic bonds, has been studied extensively for energy applications[23], chemical sensors[24], and catalysis[25]. MD simulations on hexaaminobenzene-based (HAB) 2D MOF showed that MOFs are also good candidates for water desalination[26].

Despite the great promise of water purification using 2D porous membranes, there is currently a lack of understanding of how membrane flexibility affects desalination performance. In this work, we investigate how the flexibility of nanoporous membranes affects the performance of water desalination. We first examine the physical mechanisms governing water permeability in the flexible membrane. Subsequently, we also investigate the mechanical fracture of the 2D nanoporous membranes when an out-of-plane hydrodynamic pressure is used for water desalination.

RESULTS AND DISCUSSION

Water desalination performance is investigated by performing extensive all-atom MD simulations for several promising 2D nanoporous membranes – namely, GNMs (graphene-based), CTFs (COF-based), and Cu-HAB (MOF-based) as shown in Fig. 1b-h. We assumed the membranes to be ideal and neglected atomic defects. All the tested membranes were hydrogenated. During the simulations, the edges of the membranes were constrained (Fig. 1a), and hydrodynamic pressure was applied. The desalination performance of both rigid membranes (see Fig. 2a) and flexible membranes (see Fig. 2b) was examined. Fig. 2c shows a linear increase of the number of filtered water molecules with time indicating steady-state filtration. Also, the water flux increases linearly with the applied pressure in both rigid and flexible membranes and the rejection rate is almost invariant for various RO pressures of 5 ~ 100 MPa (Supplementary Fig. 1). This data shows that the threshold pressure[27] is negligibly small, which is in line with the simulation data of Cohen-Tanugi *et al.*[28] We attribute this to the single-atom thickness and hydrophilic nature of hydrogenated pore. Thus, we used 100 MPa in most of the studies here for computational efficiency.

All tested flexible membranes show higher water flux than the rigid counterpart. This means that the flexible membrane allows faster water desalination compared to the previously reported desalination performance in rigid membranes[8,13,26,29]. We define the enhancement of water permeance as $\varepsilon_P = \left(P_{\text{flex}} - P_{\text{rigid}}\right)/P_{\text{rigid}}$, where P_{flex} and P_{rigid} are the permeance of flexible and rigid membrane, respectively. The highest enhancement ratio is 122% in Cu-HAB, and the lowest enhancement is 14% in GNM-2. Notably, we consistently observed this high rate of permeance enhancement in different conditions such as various RO pressures of 5 ~ 100 MPa (Supplementary Fig. 1), different thermodynamic ensembles, and different temperature ranges (Supplementary Fig. 2). The rejection rates in flexible membranes are lower overall (less than

11%) than the rigid membranes. GNM-0 and CTF-0 are found to be impermeable for both water and ions regardless of the flexibility of the membrane under 100 MPa. Fig. 2d and Fig. 2e show, respectively, the water flux per pore and the rejection rate as a function of the pore diameter. In both rigid and flexible membranes, the water flux per pore follows $Q \propto D^3$, which is the scaling of fluid flow through a thin orifice suggested by Sampson in 1891[30]. Overall, the flexible membranes show higher Q/D^3 values compared to that of the rigid membranes. Fig. 2e shows that the salt rejection rate drastically decreases in the regime above the critical diameter (~ 0.57 nm), which is close to the previously reported threshold diameter of 0.55 nm in the graphene nanoporous memebrane[13]. The desalination performances are summarized in Supplementary Table 1. Fig 2f shows the trade-off between the rejection rate and permeance and suggests that the maximum achievable permeance while keeping the perfect rejection rate is about $2{,}000 \sim 3{,}000\ \mathrm{kgm^{-2}h^{-1}bar^{-1}}$. Notably, we observed higher enhancement of permeance in the softer material (*i.e.,* low elastic modulus) as shown in Fig. 2g. To gain more insights into the physics, we performed further analysis as described below.

The flexible membranes undergo both the mechanical deformation and thermal fluctuations during the desalination process. To reveal how these mechanisms affect the water permeability, we considered three different scenarios: 1. flat rigid membrane with no mechanical deformation or thermal fluctuations, 2. deformed membrane without thermal fluctuations, and 3. deformed membrane with thermal fluctuations. In sub-nanometer pores, water exhibits single/double-file flow, where the radial variation of axial velocity is negligible. In this case, the flux Q can be approximated by $Q/n_\mathrm{p} = A\rho_\mathrm{w}u_\mathrm{w}$, where n_p is the number of pores, A is the area of the pore, ρ_w is the average water density in the pore, and u_w is the average velocity of water in the pore. The density distributions in Fig. 3a show that the deformed membranes without thermal fluctuations

(dashed lines) allow the water molecules to occupy a larger region compared to the undeformed counterparts (dotted lines). This enlargement effect in GNM-2 is small compared to that in CTF-1-CH_3 and Cu-HAB, owing to the relatively higher mechanical stiffness of graphene-based membranes. It should be noted that the deformation of 2D membranes involves not only the stretching of atomic bonds but also the rotation of chemical building blocks. The atomic structures of GNM-1 and CTF-1-CH_3 allow the rotation of some building blocks (see Fig. 2b where the black arrow shows the rotation of building block) and result in additional occupation of water molecules in the pore. Thus, the number of water molecules in the pore, n_{w}, is greater in GNM-1 and CTF-1-CH_3 (Fig. 3b. left) than in other membranes where the building blocks do not undergo significant rotation (*i.e.,* GNM-2, GNM-3, and Cu-HAB). The effect of deformation on the water velocity in the pore is within 20%. On the other hand, water velocity increases up to 102% in the membrane with thermal fluctuations compared to the membrane without thermal fluctuation (Fig. 3b right). This implies that a coupling between the fluctuating membrane and water molecules results in a better water permeation.

Similar phenomenon has been reported in other studies. Marbach *et al.*[6] presented a theory where the effective diffusion of the fluid confined between the fluctuating surfaces can be enhanced or reduced depending on the spectrum of surface fluctuation. Ma *et al.*[5] observed the coupling between the water transport and longitudinal vibration of carbon nanotube and showed that diffusion of confined water is considerably enhanced in the low frequency phonon mode due to the reduced friction. In granular transport, a vibrating inlet significantly enhances the granular transport breaking the clogged particles at the entrance[31] (*e.g.,* shaking the salt bottle).

To understand the physical mechanism governing enhanced velocity, we analyzed the Vibrational Density of States (VDOS) of membrane and water in the pore. VDOS is obtained from the Fourier transform of the velocity autocorrelation function, *i.e.,*

$$\mathrm{VDOS}(\omega) = \int_{-\infty}^{\infty} \langle \boldsymbol{u}(t_0 + t)\boldsymbol{u}(t_0)\rangle e^{-2\pi i\omega t} dt \tag{1}$$

where $\boldsymbol{u}(t)$ is the velocity at time t, $\langle \cdots \rangle$ denotes the ensemble and time average for various reference times, t_0, and ω is the frequency. We computed VDOS using the out-of-plane velocity component (the direction of water permeation) for both water molecule and membrane atoms, and then normalized it so that its integration over frequency is equal to unity. The ReaxFF potential utilized in this work for membrane-membrane interactions describes reasonably well the experimental phonon-modes[32] and IR spectrum[33]. Fig. 3c. shows the normalized VDOS of membrane atoms and water molecules inside the pore. The vibration of water molecules is dominated by the frequencies lower than 20 THz, where the translational modes of hydrogen bonds exhibit a peak at 1.8 THz and the intermolecular stretching and bending modes occupy the rest of the frequencies[34]. We observe that there is a significant overlap between the VDOS of Cu-HAB and that of water molecules. We hypothesize that the frequency match between the vibrating water molecules and membrane (*i.e.,* phonon-fluid coupling) improves the water permeability of the membrane. To test this hypothesis, we conducted a conceptual study by artificially vibrating the membrane with a single frequency ω_{m} and considering many such frequencies. Fig. 3d shows water permeation as a function of the frequency of the harmonically vibrating membrane (black circles) and VDOS of water molecules in the pore (red line). We observe permeance enhancement at the frequency with high VDOS of water. In other words, the frequency match between the fluctuating membrane and vibrating water molecules results in enhanced water permeation. This

phonon-fluid coupling phenomenon also explains our observation that the permeability is greater in the soft material (Fig. 2g) as the soft material exhibits low-frequency fluctuation ($\omega \sim \sqrt{E}$, where E is the elastic modulus). Furthermore, the desalination performance can be enhanced by manipulating the vibrational frequency of the membrane using doping[35] or applying strain[36]. We remark that the phonon-fluid coupling effect can be broadly applied to nanofluidic devices such as energy harvesting from salinity gradient[37], DNA sequencing[38], etc.

Applying a high RO pressure is necessary for rapid water desalination. On the other hand, applying high-pressure increases the risk of membrane failure. We tested the mechanical fracture of the membranes. The maximum deflection of the membrane (*i.e.,* δ, shown in Fig. 1a) is recorded as a function of pressure and is shown in Fig. 4a. The 2D membranes deform into an arc shape due to the hydrodynamic pressure (Fig. 1a). This shape of deformation is expected when the thickness of the membrane is much smaller than the in-plane length of the membrane, where the bending strain energy is negligible compared to the tensile strain energy[39]. In that case, the 2D in-plane stress ($\sigma^{2\mathrm{D}}$) is given by[40]

$$\sigma^{2\mathrm{D}} = \frac{p_{\mathrm{m}} L_{\mathrm{m}}}{2 \sin\theta} \tag{2}$$

where $\sigma^{2\mathrm{D}}$ is the 2D stress in units of $\mathrm{N/m}$, L_{m} is the length of the membrane, $\theta = 2 \arctan \frac{2\delta}{L_{\mathrm{m}}}$ is the half angle of cylindrical arc and p_{m} is the pressure exerted on the membrane. We directly measured the pressure exerted on the membrane and found that p_{m} is nearly equal to the applied RO pressure to within 1% error because of the slow process of water permeation in the sub-nanometer pore. In the linear elastic regime, the 2D elastic modulus is given by $E^{2\mathrm{D}} = \frac{\sigma^{2\mathrm{D}}}{\epsilon}$ in units of $\mathrm{N/m}$, where $\epsilon = \frac{\theta \sin\theta_0}{\theta_0 \sin\theta} - 1$ is the strain, $\theta_0 = 2 \arctan \frac{2\delta_0}{L_{\mathrm{m}}}$ is the initial half-angle of the

cylindrical arc, and δ_0 is the initial deformation. This linear elastic model with the plane strain assumption agrees with the MD simulation result. The elastic modulus of graphene-based membrane (59.5 ~ 108.8 N/m) is higher than that of CTF-1-CH3 (40.8 N/m) and Cu-HAB (34.0 N/m), but is much smaller than that of pristine graphene (340 N/m) due to the porous structure[8]. Fig. 4d-h shows the failure initiation due to the most fragile bond in the 2D membranes considered in this work. The ultimate stress of membranes is shown in Fig. 4b. Notably, the ultimate stress of Cu-HAB (1.0 N/m) is about an order of magnitude smaller than that of GNMs (9.4 ~ 13.3 N/m) owing to the weak Cu-N bond compared to the C-C bond. The computed mechanical properties and desalination performance are summarized in Supplementary Table 1. According to equation (2), the ultimate pressure (p_{ult}) follows the scaling, $p_{\mathrm{ult}} \propto \frac{\sigma_{\mathrm{ult}}}{L_{\mathrm{m}}}$, where σ_{ult} is the ultimate stress of the membrane. Hence, the desalination membrane with a smaller L_{m} endures higher RO pressure. Fig. 4c shows the maximum endurable pressure (Factor of safety = 1) of 2D desalination membranes as a function of L_{m}. At the typical RO pressure of 5 MPa, the GNMs can be used with $L_{\mathrm{m}} \lesssim 400$ nm without breakage, while Cu-HAB can be used for $L_{\mathrm{m}} \lesssim 30$ nm. This indicates that the GNMs withstand a higher RO pressure on the same supporting structure (*e.g.,* carbon nanotube network on a polyethylene terephthalate substrate[15]) than Cu-HAB and CTF-1-CH_3.

CONCLUSION

In this work, we investigated water desalination using 2D flexible membrane considering the coupled dynamics between the membrane and water. The flexible 2D membranes involve significant mechanical deformation and thermal fluctuations during the desalination process. The water permeation is enhanced up to 122% due to the flexibility of the membrane involving the mechanical deformation and thermal fluctuations. The mechanical deformation enlarges the accessible diameter of the pore increasing the water flux. The thermal fluctuations of the

membrane increase the speed of water transport. To understand the mechanism of increased water velocity arising from the membrane fluctuation, we analyzed the vibrational density of states over various frequencies. Our studies showed that a frequency match between vibrating water molecules and the fluctuating membrane (phonon-fluid coupling at the water-membrane interface) substantially enhances the water permeation. The mechanical fracture tests show that the mechanical strength of graphene-based membrane is 1,060 ~ 1,540 % stronger than Cu-HAB (MOF) and 252 ~ 367% stronger than CTF-1-CH_3 (COF). The results presented in this work will be fundamental for membrane applications such as energy harvesting from the salinity gradient[37], molecular separation[20], DNA detection/translocation[38], energy storage[19,23], catalyst[25], and chemical sensors[24].

METHODS

We considered systems with the desalination membrane immersed in 0.55M NaCl solution, which offers conditions similar to seawater. The size of the membrane ranges from 6 nm to 10 nm in the x dimension and 1 nm to 8 nm in the y dimension, depending on the system, which is considerably larger compared to earlier works[8,21,26,29]. Periodic boundary condition is employed in all the three directions. Our studies confirmed that our system exhibits an ignorable size effect on both water desalination performance and mechanical fracture test. We used salt ions modeled by LJ potentials described in Joung *et al.*[41] and the flexible simple point-charge water model[42]. The carbon-water interatomic potential is adopted from Wu and Aluru[43]. The interactions among the membrane atoms are modeled using the ReaxFF forcefield[44] (Wood *et al.*[33] for GNMs and CTFs, and Monti *et al.*[45] for Cu-HAB). The rest of the membrane-fluid force fields are modeled using the non-reactive LJ and Coulombic potential and the Lorentz-Berthelot mixing rule with pair potential parameters proposed by Siu *et al.*[46] for hydrogen, Jorgensen *et al.*[47] for nitrogen, and Heinz *et al.*[48] for copper. The diameter of the pore was determined based on the accessible area of water using the LJ diameter of oxygen (Supplementary Fig. 8). The temperature of the system is maintained at 298K with Nosé-Hoover thermostat. The partial charges of membrane atoms are computed by the charge equilibration (QEq) method[49] at the initial stage of the MD simulation (after the energy minimization). The equilibrated partial charges are then fixed during the simulation (summarized in Supplementary Fig. 7). The long-range electrostatic potential is calculated by using the PPPM method[50]. The cut-off distance of LJ potential is set to be 1.2 nm. The atomic trajectories are integrated in NVT ensemble with 0.5 fs time step, which shows a good stability with ReaxFF force field during fracture test[51]. For desalination of water, a hydrostatic pressure (5 MPa ~ 100 MPa) is applied to the fluid molecules in a 1 nm thick box at the edge of the simulation domain. For the

radial distribution of density and velocity in the pore, we considered a pore located in the center of the membrane and 2Å long cylindrical bins. For the mechanical fracture test, we applied an increasing pressure with a rate of 2 MPa/ps. For equilibrium MD simulation, no pressure was applied. For activated vibrating membrane, we considered Cu-HAB and the membrane is harmonically vibrated in the out-of-plane direction. The average kinetic energy per atom of oscillating membrane set to be the thermal energy $\frac{k_B T}{2}$, where k_B is the Boltzmann constant and T is the temperature. For fast computation of atomic trajectory, the GPU-assisted accelerated computation[52] is used. For MD simulation, the Large-scale Atomic/Molecular Massively Parallel Simulator (LAMMPS)[53] is used. For visualization, Open Visualization Tool (OVITO)[54] is used.

AUTHOR INFORMATION

Corresponding Author

*E-mail: aluru@illinois.edu

Author Contributions

Y.N performed simulations, analysis, and wrote the manuscript under the guidance of N.A.

ACKNOWLEDGMENTS

The work on graphene membranes was supported by the Center for Enhanced Nanofluidic Transport (CENT), an Energy Frontier Research Center funded by the U.S. Department of Energy, Office of Science, Basic Energy Sciences (Award # DE-SC0019112). All other aspects of this work were supported by the National Science Foundation under Grant 2140225. The computing power is provided by the Extreme Science and Engineering Discovery Environment (XSEDE) granted by National Science Foundation (NSF) Grant No. OCI1053575 and Blue Waters supercomputing center, awarded by the state of Illinois and NSF, OCI-0725070, ACI-1238993.

REFERENCES

(1) Bernèche, S.; Roux, B. Energetics of Ion Conduction through the K + Channel. *Nature* **2001**, *414* (6859), 73–77. https://doi.org/10.1038/35102067.

(2) Noskov, S. Y.; Bernèche, S.; Roux, B. Control of Ion Selectivity in Potassium Channels by Electrostatic and Dynamic Properties of Carbonyl Ligands. *Nature* **2004**, *431* (7010), 830–834. https://doi.org/10.1038/nature02943.

(3) Kohen, A.; Cannio, R.; Bartolucci, S.; Klinman, J. P.; Klinman, J. P. Enzyme Dynamics and Hydrogen Tunnelling in a Thermophilic Alcohol Dehydrogenase. *Nature* **1999**, *399* (6735), 496–499. https://doi.org/10.1038/20981.

(4) Fetzer, R.; Rauscher, M.; Seemann, R.; Jacobs, K.; Mecke, K. Thermal Noise Influences Fluid Flow in Thin Films during Spinodal Dewetting. *Phys. Rev. Lett.* **2007**, *99* (11), 114503. https://doi.org/10.1103/PhysRevLett.99.114503.

(5) Ma, M.; Grey, F.; Shen, L.; Urbakh, M.; Wu, S.; Liu, J. Z.; Liu, Y.; Zheng, Q. Water Transport inside Carbon Nanotubes Mediated by Phonon-Induced Oscillating Friction. *Nature Nanotechnology* **2015**, *10* (8), 692–695. https://doi.org/10.1038/nnano.2015.134.

(6) Marbach, S.; Dean, D. S.; Bocquet, L. Transport and Dispersion across Wiggling Nanopores. *Nature Physics* **2018**, *14* (11), 1108–1113. https://doi.org/10.1038/s41567-018-0239-0.

(7) Moseler, M.; Landman, U. Formation, Stability, and Breakup of Nanojets. *Science* **2000**, *289* (5482), 1165–1169. https://doi.org/10.1126/science.289.5482.1165.

(8) Cohen-Tanugi, D.; Grossman, J. C. Mechanical Strength of Nanoporous Graphene as a Desalination Membrane. *Nano Lett.* **2014**, *14* (11), 6171–6178. https://doi.org/10.1021/nl502399y.

(9) Roark, R. J.; Young, W. C.; Budynas, R. G. *Roark's Formulas for Stress and Strain*, 7th ed.; McGraw-Hill: New York, 2002.

(10) Ahmadpoor, F.; Wang, P.; Huang, R.; Sharma, P. Thermal Fluctuations and Effective Bending Stiffness of Elastic Thin Sheets and Graphene: A Nonlinear Analysis. *Journal of the Mechanics and Physics of Solids* **2017**, *107*, 294–319. https://doi.org/10.1016/j.jmps.2017.07.011.

(11) Meyer, J. C.; Geim, A. K.; Katsnelson, M. I.; Novoselov, K. S.; Booth, T. J.; Roth, S. The Structure of Suspended Graphene Sheets. *Nature* **2007**, *446* (7131), 60–63. https://doi.org/10.1038/nature05545.

(12) Fasolino, A.; Los, J. H.; Katsnelson, M. I. Intrinsic Ripples in Graphene. *Nature Materials* **2007**, *6* (11), 858–861. https://doi.org/10.1038/nmat2011.

(13) Cohen-Tanugi, D.; Grossman, J. C. Water Desalination across Nanoporous Graphene. *Nano Lett.* **2012**, *12* (7), 3602–3608. https://doi.org/10.1021/nl3012853.

(14) Nightingale, E. R. Phenomenological Theory of Ion Solvation. Effective Radii of Hydrated Ions. *J. Phys. Chem.* **1959**, *63* (9), 1381–1387. https://doi.org/10.1021/j150579a011.

(15) Yang, Y.; Yang, X.; Liang, L.; Gao, Y.; Cheng, H.; Li, X.; Zou, M.; Ma, R.; Yuan, Q.; Duan, X. Large-Area Graphene-Nanomesh/Carbon-Nanotube Hybrid Membranes for Ionic and Molecular Nanofiltration. *Science* **2019**, *364* (6445), 1057–1062. https://doi.org/10.1126/science.aau5321.

(16) Moreno, C.; Vilas-Varela, M.; Kretz, B.; Garcia-Lekue, A.; Costache, M. V.; Paradinas, M.; Panighel, M.; Ceballos, G.; Valenzuela, S. O.; Peña, D.; Mugarza, A. Bottom-up Synthesis

of Multifunctional Nanoporous Graphene. *Science* **2018**, *360* (6385), 199–203. https://doi.org/10.1126/science.aar2009.

(17) Côté, A. P.; Benin, A. I.; Ockwig, N. W.; O'Keeffe, M.; Matzger, A. J.; Yaghi, O. M. Porous, Crystalline, Covalent Organic Frameworks. *Science* **2005**, *310* (5751), 1166–1170. https://doi.org/10.1126/science.1120411.

(18) Zhong, Y.; Cheng, B.; Park, C.; Ray, A.; Brown, S.; Mujid, F.; Lee, J.-U.; Zhou, H.; Suh, J.; Lee, K.-H.; Mannix, A. J.; Kang, K.; Sibener, S. J.; Muller, D. A.; Park, J. Wafer-Scale Synthesis of Monolayer Two-Dimensional Porphyrin Polymers for Hybrid Superlattices. *Science* **2019**, *366* (6471), 1379–1384. https://doi.org/10.1126/science.aax9385.

(19) Mandal, A. K.; Mahmood, J.; Baek, J.-B. Two-Dimensional Covalent Organic Frameworks for Optoelectronics and Energy Storage. *ChemNanoMat* **2017**, *3* (6), 373–391. https://doi.org/10.1002/cnma.201700048.

(20) Yuan, S.; Li, X.; Zhu, J.; Zhang, G.; Puyvelde, P. V.; Bruggen, B. V. der. Covalent Organic Frameworks for Membrane Separation. *Chemical Society Reviews* **2019**, *48* (10), 2665–2681. https://doi.org/10.1039/C8CS00919H.

(21) Lin, L.-C.; Choi, J.; C. Grossman, J. Two-Dimensional Covalent Triazine Framework as an Ultrathin-Film Nanoporous Membrane for Desalination. *Chemical Communications* **2015**, *51* (80), 14921–14924. https://doi.org/10.1039/C5CC05969K.

(22) Feng, D.; Lei, T.; Lukatskaya, M. R.; Park, J.; Huang, Z.; Lee, M.; Shaw, L.; Chen, S.; Yakovenko, A. A.; Kulkarni, A.; Xiao, J.; Fredrickson, K.; Tok, J. B.; Zou, X.; Cui, Y.; Bao, Z. Robust and Conductive Two-Dimensional Metal−organic Frameworks with Exceptionally High Volumetric and Areal Capacitance. *Nature Energy* **2018**, *3* (1), 30–36. https://doi.org/10.1038/s41560-017-0044-5.

(23) Wang, H.; Zhu, Q.-L.; Zou, R.; Xu, Q. Metal-Organic Frameworks for Energy Applications. *Chem* **2017**, *2* (1), 52–80. https://doi.org/10.1016/j.chempr.2016.12.002.

(24) Kreno, L. E.; Leong, K.; Farha, O. K.; Allendorf, M.; Van Duyne, R. P.; Hupp, J. T. Metal–Organic Framework Materials as Chemical Sensors. *Chem. Rev.* **2012**, *112* (2), 1105–1125. https://doi.org/10.1021/cr200324t.

(25) Lee, J.; K. Farha, O.; Roberts, J.; A. Scheidt, K.; T. Nguyen, S.; T. Hupp, J. Metal–Organic Framework Materials as Catalysts. *Chemical Society Reviews* **2009**, *38* (5), 1450–1459. https://doi.org/10.1039/B807080F.

(26) Cao, Z.; Liu, V.; Barati Farimani, A. Water Desalination with Two-Dimensional Metal–Organic Framework Membranes. *Nano Lett.* **2019**, *19* (12), 8638–8643. https://doi.org/10.1021/acs.nanolett.9b03225.

(27) Xu, F.; Wei, M.; Zhang, X.; Song, Y.; Zhou, W.; Wang, Y. How Pore Hydrophilicity Influences Water Permeability? *Research* **2019**, *2019*. https://doi.org/10.34133/2019/2581241.

(28) Cohen-Tanugi, D.; Grossman, J. C. Water Permeability of Nanoporous Graphene at Realistic Pressures for Reverse Osmosis Desalination. *J. Chem. Phys.* **2014**, *141* (7), 074704. https://doi.org/10.1063/1.4892638.

(29) Heiranian, M.; Farimani, A. B.; Aluru, N. R. Water Desalination with a Single-Layer MoS 2 Nanopore. *Nature communications* **2015**, *6*, 8616.

(30) Sampson, R. A.; Greenhill, A. G. XII. On Stokes's Current Function. *Philosophical Transactions of the Royal Society of London. (A.)* **1891**, *182*, 449–518. https://doi.org/10.1098/rsta.1891.0012.

(31) Wen, P.; Zheng, N.; Nian, J.; Li, L.; Shi, Q. Flux of Granular Particles through a Shaken Sieve Plate. *Scientific Reports* **2015**, *5* (1), 9880. https://doi.org/10.1038/srep09880.
(32) Diao, C.; Dong, Y.; Lin, J. Reactive Force Field Simulation on Thermal Conductivities of Carbon Nanotubes and Graphene. *International Journal of Heat and Mass Transfer* **2017**, *112*, 903–912. https://doi.org/10.1016/j.ijheatmasstransfer.2017.05.036.
(33) Wood, M. A.; van Duin, A. C. T.; Strachan, A. Coupled Thermal and Electromagnetic Induced Decomposition in the Molecular Explosive AHMX; A Reactive Molecular Dynamics Study. *J. Phys. Chem. A* **2014**, *118* (5), 885–895. https://doi.org/10.1021/jp406248m.
(34) Yagasaki, T.; Saito, S. A Novel Method for Analyzing Energy Relaxation in Condensed Phases Using Nonequilibrium Molecular Dynamics Simulations: Application to the Energy Relaxation of Intermolecular Motions in Liquid Water. *J. Chem. Phys.* **2011**, *134* (18), 184503. https://doi.org/10.1063/1.3587105.
(35) Giannozzi, P.; Andreoni, W. Effects of Doping on the Vibrational Properties of ${C}_{60}$ from First Principles: ${K}_{6}{C}_{60}$. *Phys. Rev. Lett.* **1996**, *76* (26), 4915–4918. https://doi.org/10.1103/PhysRevLett.76.4915.
(36) Wang, Y.; Cong, C.; Qiu, C.; Yu, T. Raman Spectroscopy Study of Lattice Vibration and Crystallographic Orientation of Monolayer MoS2 under Uniaxial Strain. *Small* **2013**, *9* (17), 2857–2861. https://doi.org/10.1002/smll.201202876.
(37) Feng, J.; Graf, M.; Liu, K.; Ovchinnikov, D.; Dumcenco, D.; Heiranian, M.; Nandigana, V.; Aluru, N. R.; Kis, A.; Radenovic, A. Single-Layer MoS2 Nanopores as Nanopower Generators. *Nature* **2016**, *536* (7615), 197. https://doi.org/10.1038/nature18593.
(38) Traversi, F.; Raillon, C.; Benameur, S. M.; Liu, K.; Khlybov, S.; Tosun, M.; Krasnozhon, D.; Kis, A.; Radenovic, A. Detecting the Translocation of DNA through a Nanopore Using Graphene Nanoribbons. *Nature Nanotech* **2013**, *8* (12), 939–945. https://doi.org/10.1038/nnano.2013.240.
(39) Xiang, Y.; Chen, X.; Vlassak, J. J. Plane-Strain Bulge Test for Thin Films. *Journal of Materials Research* **2005**, *20* (9), 2360–2370. https://doi.org/10.1557/jmr.2005.0313.
(40) Xiang, Y. Plasticity in Cu Thin Films: An Experimental Investigation of the Effect of Microstructure, 2006.
(41) Joung, I. S.; Cheatham, T. E. Determination of Alkali and Halide Monovalent Ion Parameters for Use in Explicitly Solvated Biomolecular Simulations. *The Journal of Physical Chemistry. B* **2008**. https://doi.org/10.1021/jp8001614.
(42) Wu, Y.; Tepper, H. L.; Voth, G. A. Flexible Simple Point-Charge Water Model with Improved Liquid-State Properties. *J. Chem. Phys.* **2006**, *124* (2), 024503. https://doi.org/10.1063/1.2136877.
(43) Wu, Y.; Aluru, N. R. Graphitic Carbon–Water Nonbonded Interaction Parameters. *J. Phys. Chem. B* **2013**, *117* (29), 8802–8813. https://doi.org/10.1021/jp402051t.
(44) van Duin, A. C. T.; Dasgupta, S.; Lorant, F.; Goddard, W. A. ReaxFF: A Reactive Force Field for Hydrocarbons. *J. Phys. Chem. A* **2001**, *105* (41), 9396–9409. https://doi.org/10.1021/jp004368u.
(45) Monti, S.; Li, C.; Carravetta, V. Reactive Dynamics Simulation of Monolayer and Multilayer Adsorption of Glycine on Cu(110). *J. Phys. Chem. C* **2013**, *117* (10), 5221–5228. https://doi.org/10.1021/jp312828d.

(46) Siu, S. W. I.; Pluhackova, K.; Böckmann, R. A. Optimization of the OPLS-AA Force Field for Long Hydrocarbons. *J. Chem. Theory Comput.* **2012**, *8* (4), 1459–1470. https://doi.org/10.1021/ct200908r.
(47) Jorgensen, W. L.; Maxwell, D. S.; Tirado-Rives, J. Development and Testing of the OPLS All-Atom Force Field on Conformational Energetics and Properties of Organic Liquids. *J. Am. Chem. Soc.* **1996**, *118* (45), 11225–11236. https://doi.org/10.1021/ja9621760.
(48) Heinz, H.; Vaia, R. A.; Farmer, B. L.; Naik, R. R. Accurate Simulation of Surfaces and Interfaces of Face-Centered Cubic Metals Using 12−6 and 9−6 Lennard-Jones Potentials. *The Journal of Physical Chemistry C* **2008**, *112* (44), 17281–17290. https://doi.org/10.1021/jp801931d.
(49) Rappe, A. K.; Goddard, W. A. Charge Equilibration for Molecular Dynamics Simulations. *J. Phys. Chem.* **1991**, *95* (8), 3358–3363. https://doi.org/10.1021/j100161a070.
(50) Hockney, R. W.; Eastwood, J. W. Computer Simulation Using Particles. *Computer Simulation Using Particles, New York: McGraw-Hill, 1981* **1981**.
(51) Jensen, B. D.; Wise, K. E.; Odegard, G. M. The Effect of Time Step, Thermostat, and Strain Rate on ReaxFF Simulations of Mechanical Failure in Diamond, Graphene, and Carbon Nanotube. *Journal of Computational Chemistry* **2015**, *36* (21), 1587–1596. https://doi.org/10.1002/jcc.23970.
(52) Brown, W. M.; Wang, P.; Plimpton, S. J.; Tharrington, A. N. Implementing Molecular Dynamics on Hybrid High Performance Computers – Short Range Forces. *Computer Physics Communications* **2011**, *182* (4), 898–911. https://doi.org/10.1016/j.cpc.2010.12.021.
(53) Plimpton, S. Fast Parallel Algorithms for Short-Range Molecular Dynamics. *Journal of Computational Physics* **1995**, *117* (1), 1–19. https://doi.org/10.1006/jcph.1995.1039.
(54) Stukowski, A. Visualization and Analysis of Atomistic Simulation Data with OVITO–the Open Visualization Tool. *Modelling and Simulation in Materials Science and Engineering* **2010**, *18*, 015012. https://doi.org/10.1088/0965-0393/18/1/015012.

LIST OF FIGURES

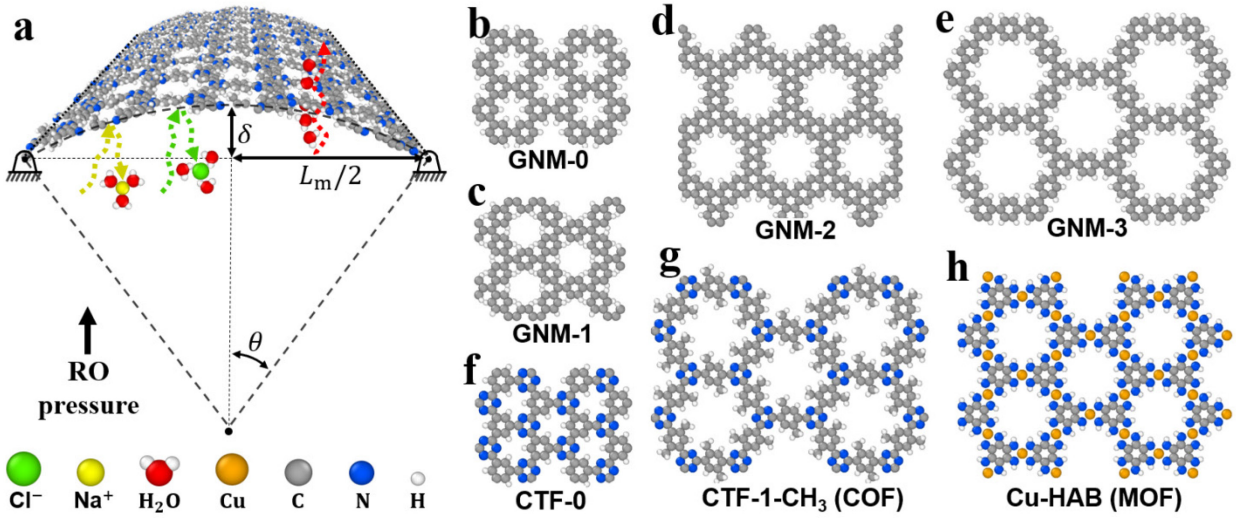

Figure 1 | Water desalination using 2D flexible porous membranes. a, Schematic of water desalination using a 2D flexible membrane with constrained edges. **b-h**, Atomic structure of 2D porous membranes considered in this work.

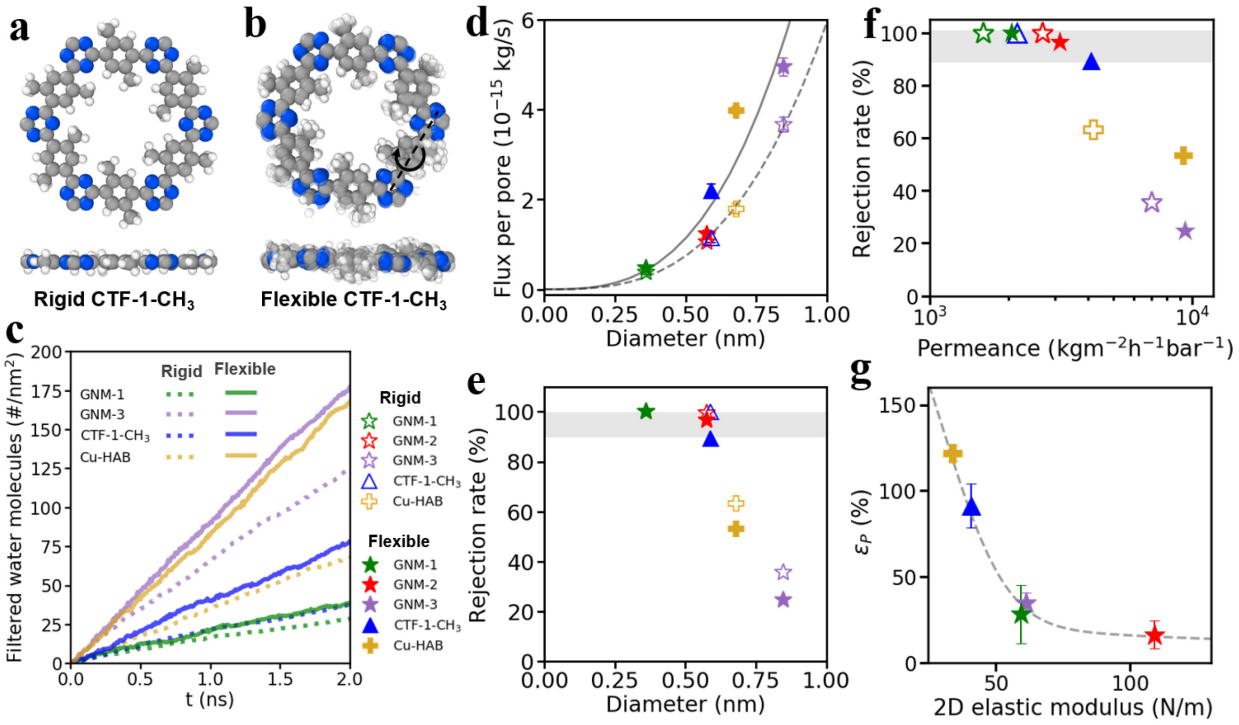

Figure 2 | Desalination performance of flexible membranes. a, Rigid CTF-1-CH_3 (top view and side view). **b**, Flexible CTF-1-CH_3. The black arrow and dashed line represent the rotation of the building block and its pivot, respectively. **c**, Filtered water molecules over time. **d**, Water permeation per pore as a function of the pore diameter. The lines represent the least-squares fitting curve using $Q \propto D^3$ scaling (dashed line: rigid membranes and solid line: flexible membranes). The error is the standard error of several sets of fluxes obtained during 1 ns. **e**, Rejection rate for various pore diameters. The gray shaded area represents the rejection rate over 90%. **f**, The overall desalination performance and the trade-off between water permeance and rejection rate. **g**, The enhancement of water permeance (defined in the manuscript) as a function of the elastic modulus of the membrane. The error bar represents the error of flux in flexible membrane divided by the flux in the rigid membrane.

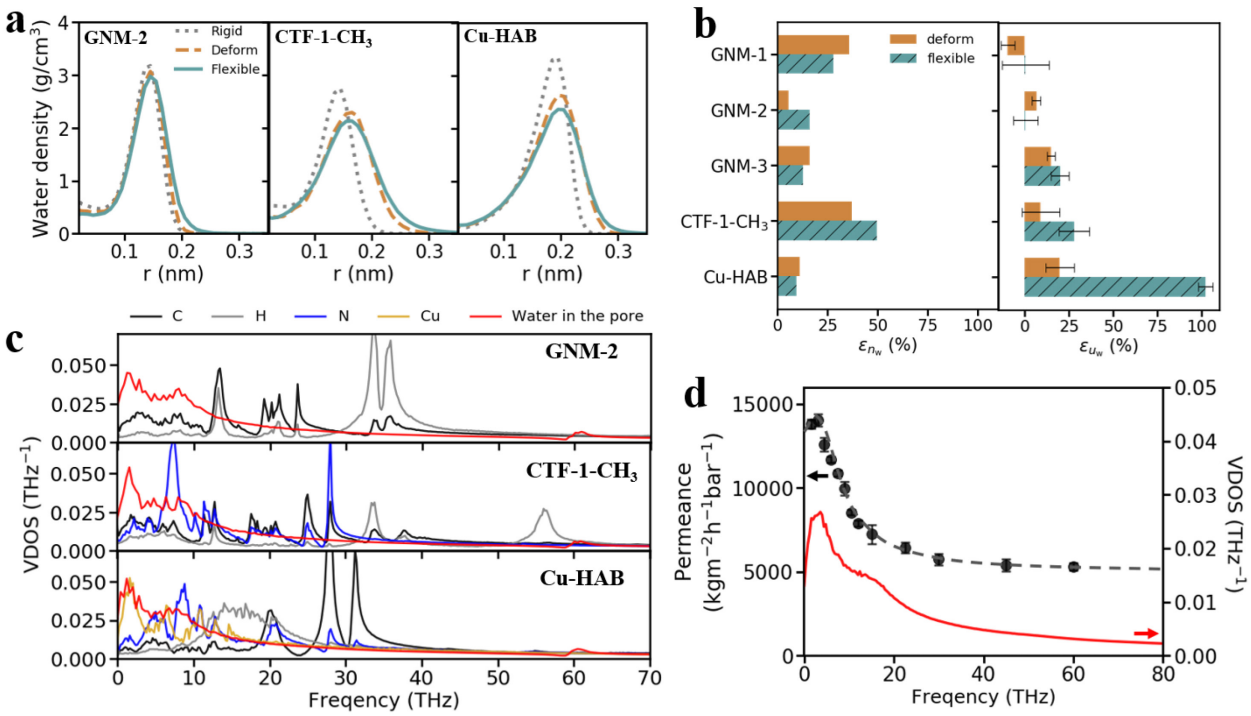

Figure 3 | Dynamics of membrane and water molecules inside the nanopore. a, Water density as a function of the distance from the pore center. **b,** (Left) Increment ratio of average number of water molecules in the nanopore. (Right) The percentage increase of water velocity in the pore. **c,** VDOS of membrane atoms and water molecules in the pore. **d,** Enhanced water permeation in the harmonically oscillating membrane at single frequency (black circle). VDOS of water molecules inside the pore (red line). In the plots here, "Deform" refers to the case where the membrane undergoes deformation, but thermal fluctuations are suppressed and "Flexible" refers to the case where both membrane deformation and thermal fluctuations are accounted for.

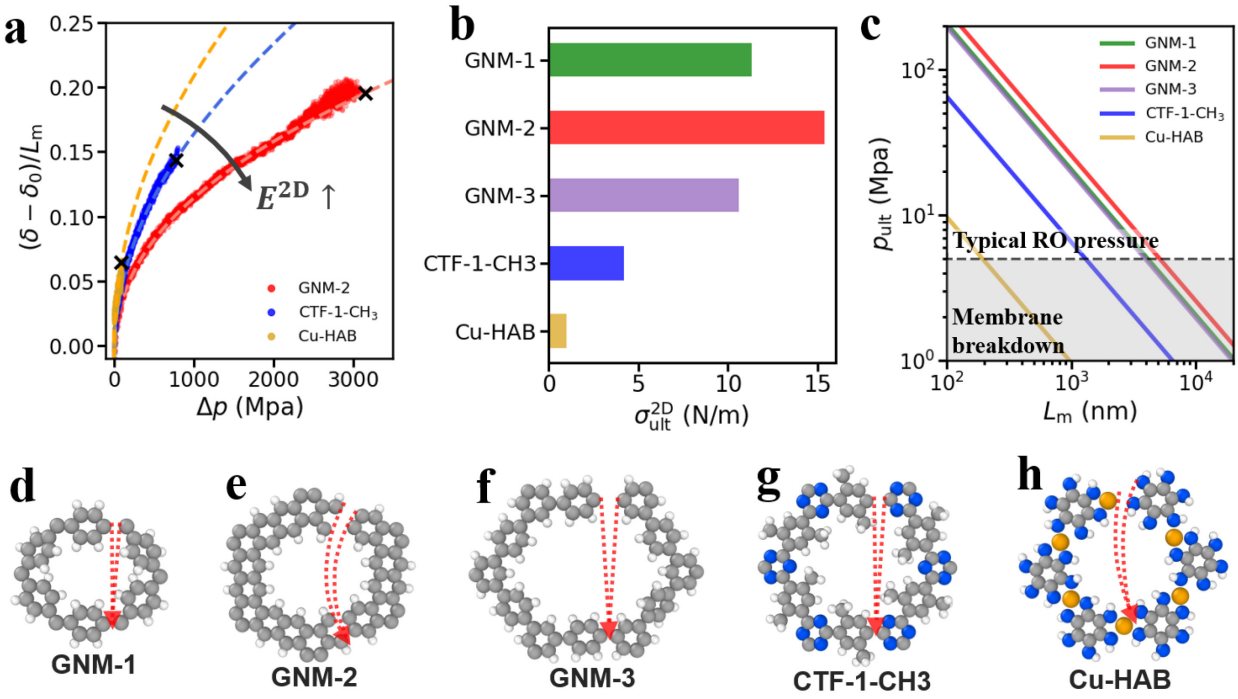

Figure 4 | Failure of 2D membranes under out-of-plane hydrodynamic pressure. a, Maximum deflection *versus* the applied pressure. δ_0 is the initial deformation as the intrinsic ripples unfold. The symbol '×' indicates the failure or mechanical breakdown of the membrane. **b**, Ultimate stress of the 2D membranes considered in this work. **c**, Ultimate RO pressure as a function of the membrane length. The gray shaded area indicates the membrane breakdown under a typical RO pressure of 5 MPa. **d-h**, Fracture samples and the direction of crack propagation (illustrated in dashed red arrow).

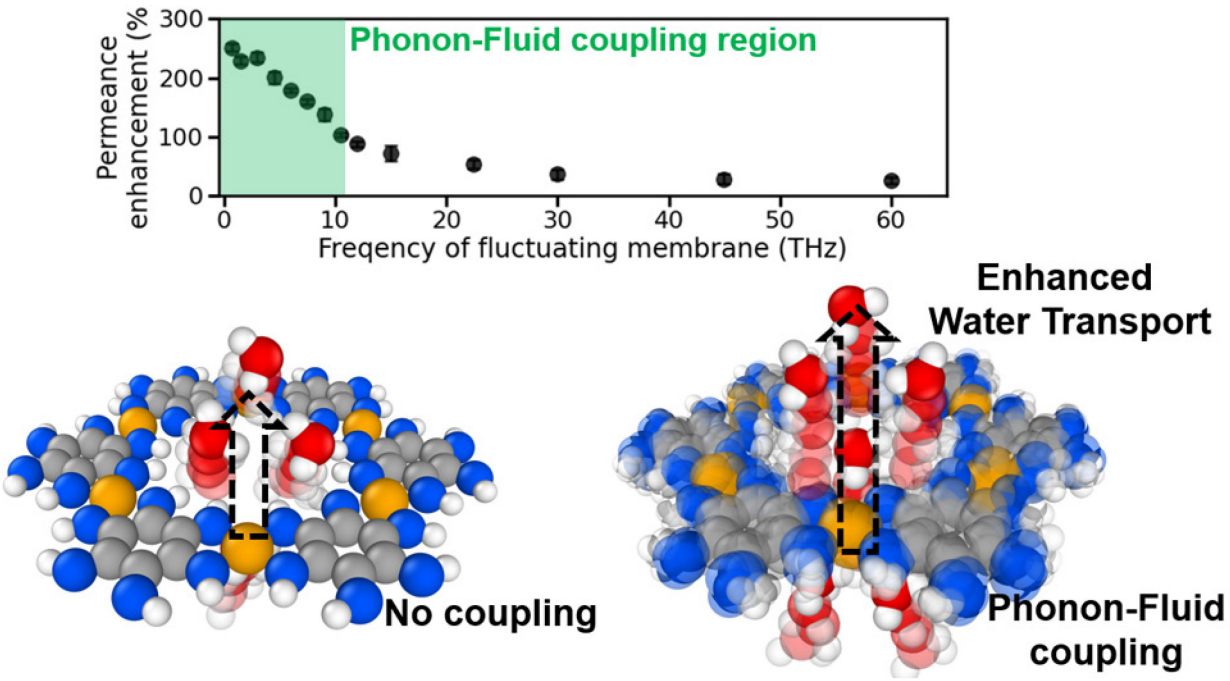

TOC graphics for Table of Contents Only